Scilight

Materials and Sustainability
https://www.sciltp.com/journals/matsus

Article

Hierarchical Porous Carbon-Carbon Dot Architecture as a High Energy Density Cathode for Lithium-Metal Capacitors

Gayathry Ganesh [1,2], Gokul Raj Deivendran [3], Vaishak Sunil [1,2], Izan Izwan Misnon [1,2], Chun-Chen Yang [3,4] and Rajan Jose [1,2,3,*]

[1] Center for Advanced Intelligent Materials, Universiti Malaysia Pahang Al-Sultan Abdullah, Kuantan 26300, Malaysia
[2] Faculty of Industrial Sciences and Technology, Universiti Malaysia Pahang Al-Sultan Abdullah, Kuantan 26300, Malaysia
[3] Battery Research Center of Green Energy, Ming Chi University of Technology, New Taipei City 243303, Taiwan
[4] Department of Chemical Engineering, Ming Chi University of Technology, New Taipei City 243303, Taiwan
* Correspondence: rjose@umpsa.edu.my or rjose@mcut.mail.edu.tw

How To Cite: Ganesh, G.; Deivendran, G.R.; Sunil, V.; et al. Hierarchical Porous Carbon-Carbon Dot Architecture as a High Energy Density Cathode for Lithium-Metal Capacitors. *Materials and Sustainability* **2025**, *1*(1), 7. https://doi.org/10.53941/matsus.2025.100007.

Received: 8 December 2024
Revised: 19 March 2025
Accepted: 24 March 2025
Published: 26 March 2025

Abstract: Hybrid devices such as lithium-metal capacitors (LMC) are in rising demand and can simultaneously meet the requirements of energy storage devices with superior specific energy and high specific power. LMCs combine a lithium anode with high specific energy and an activated carbon cathode with high specific power. Biomass-derived porous carbon (BC) is an ideal candidate as cathode material and stands out for its tuneable porosity, sustainability, and low cost. However, the inherent limitations of BC in delivering optimal electrochemical performance necessitate using additives with superior electronic conductivity. In this study, we introduce functionalized carbon quantum dots (f-CDs), synthesized from biomass, as an effective additive to enhance the performance of BC. The physicochemical and electrochemical figures of merit of BC integrated with 7 wt.% f-CDs (BC@f-CD) were systematically compared with BC modified with 0.4 wt.% single walled carbon nanotube (BC@s-CNT). Electrochemical evaluations revealed that BC@f-CD exhibited a superior specific capacitance of approximately 191 $F \cdot g^{-1}$ within a 2–4.3 V voltage window. The nano-sized dimensions and functional groups of f-CDs significantly improved performance, enabling a remarkable 111% increase in specific energy. Additionally, BC@f-CD demonstrated excellent cycling stability, retaining ~86% of its initial capacity after 5000 cycles, outperforming traditional lithium-metal batteries. This study underscores the potential of f-CDs as a cost-effective and efficient alternative additive to s-CNTs that can enhance the performance of LMCs, providing a sustainable solution for advanced energy storage applications.

Keywords: carbon dots; biomass activated carbon; lithium-ion storage; lithium-metal anode

1. Introduction

Lithium-ion batteries (LIBs) have been in the market as a forefront energy storage device for powering portable electronics and electric vehicles due to their high specific energy, low self-discharge, and high open circuit voltage [1,2]. Despite these advantages, the demand for higher energy densities, lower power densities, and shorter cycle lives of LIBs is seeking further research for improvement. The conventional graphite anode in LIBs has nearly attained its theoretical specific energy of ~350 $Wh \cdot kg^{-1}$ [3]. In this context, lithium-metal batteries (LMBs) with lithium metal as an anode are considered the holy grail with several merits, such as the highest theoretical gravimetric capacity, lowest redox potential, and low density [4,5]. Engineering the Li-metal interface through surface modification methods, regulating the initial coulombic efficiency, and adopting solid-state electrolytes have proven effective in preventing Li dendrite formation and reducing volume changes [6]. Further, these properties allow for substantial improvements in rate capabilities by permitting Lithium to be directly deposited on the anode, which, combined with the suitable electrolyte, enables the design of anode-less architectures that save on materials and manufacturing costs while improving energy density. These advancements have made lithium metal a viable option as an anode, advancing beyond the traditional concept of "half-cells" that use a Lithium-metal counter electrode, paving the way for advanced high-energy LMBs. However, the intercalation mechanism in the cathode prevents batteries from achieving high power densities.

The relatively new concept of lithium-metal capacitors (LMCs) has emerged to address these limitations, combining a lithium-metal anode with a capacitive cathode to achieve high specific energy and power simultaneously [7–13]. LMCs offer several advantages, including a superior voltage window, which is attributed to the lowest redox potential and highest specific capacity of Lithium [9]. They address the mismatch in anode-cathode kinetics commonly seen in conventional lithium-ion capacitors by enabling reversible and rapid lithium plating and stripping [11,13]. Moreover, LMCs eliminate the need for pre-lithiation, simplifying their operation and improving practicality. Research on LMCs is emerging, and only a few studies have been published. These studies include propositions of highly capacitive activated carbon (AC) cathode, Lithium-metal anode deposited on gold-coated carbon cloth, fluorinated electrolyte, the introduction of a controlled amount of polysulfides into ether-based electrolytes and novel gel polymer electrolyte [7–13]. The study using a 3D AC scaffold yielded a superior specific energy of over 633 $\text{Wh}\cdot\text{kg}^{-1}$ and a high specific power of 15.3 $\text{kW}\cdot\text{kg}^{-1}$ [11]. However, this study involves energy-intensive and material-intensive processes, as the cathodes are carbon-derived from synthetic polymers. An alternative is employing biomass-derived carbon, which can be synthesized by upcycling the biomass that otherwise ends in landfills. A study showed rice husk as a precursor for biomass-derived activated carbon (BC) could deliver a specific capacitance of 140 $\text{F}\cdot\text{g}^{-1}$ and a specific energy of 35 $\text{Wh}\cdot\text{kg}^{-1}$ in a voltage window of 2.8–4.2V [7]. However, this performance is far inferior to that of synthetic AC. Incorporating metal oxides like Mn_2CoO_3 nanoflowers [14] and TiO_2 flowers [15] or coating cobalt thin film [16] on porous BC were studied to improve the performance. Though the electrochemical performance is higher than the bare carbon, the capacitance retention is studied only for 500 cycles. Moreover, using such metal oxides is undesirable as they are mined through unsustainable techniques and retain high cost. A recent study with coconut rachis as BC shows that compositing single-walled carbon nanotube (s-CNT) improves electrochemical performance [13]. Adding 0.4 wt.%, s-CNT improved the specific capacitance up to 22% to reach ~188 $\text{F}\cdot\text{g}^{-1}$ at 0.1 $\text{A}\cdot\text{g}^{-1}$ and a specific energy of 208 $\text{Wh}\cdot\text{kg}^{-1}$ in a potential window of 2–4 V. However, additives such as s-CNTs are undesirable due to their toxicity, high cost, purity issues, and anisotropic behaviour, which lowers the electrochemical performance [17–20].

Among the several carbon additives studied, carbon dots (CDs) have gained significant attention due to their nano dimensions, surface functional groups, high conductivity, ease of synthesis, nontoxicity, and lower costs [21]. CDs are studied as electrode and electrolyte additives in LIBs, supercapacitors, and LICs [22–27]. For the first time, the effect of CDs on the electrochemical properties of LMCs is studied. In this study, we chose surface-modified BC (Figure 1a) as cathode material for LMC, whose inferior surface and electronic properties delivered a specific capacitance of ~90 $\text{F}\cdot\text{g}^{-1}$ at 0.1 $\text{A}\cdot\text{g}^{-1}$. Functionalized carbon dots (f-CDs) derived from palm kernel shells were introduced to BC to improve the performance using a sustainable and low-cost additive. The nano dimension and functional groups of f-CDs played a crucial role in improving the specific surface area, reducing resistance, and increasing the ionic conductivity of BC. The figures of merit of f-CD incorporated BC were compared against commercially procured s-CNT (Figure 1b,c) by following the procedure in the prior literature [13]. The f-CDs were found to have a superior influence on the electrochemical performance metrics of BC than the s-CNTs, resulting in a maximum specific energy of 281 $\text{Wh}\cdot\text{kg}^{-1}$.

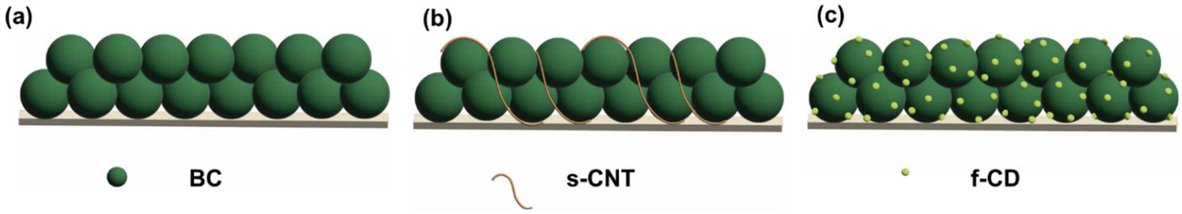

Figure 1. Schematic representation of the three cathode compositions studied. (**a**) BC (**b**) BC wrapped in s-CNT and (**c**) BC decorated with f-CDs.

2. Materials and Methods

2.1. Synthesis of Nitrogen-Doped CDs

The synthesis of BC and f-CD follows the protocol published in our previous studies [27,28]. Briefly, BC was prepared by functionalizing AC from palm kernel shells (PKS) through nitric acid (R&M chemicals, Cardiff, UK) refluxing at 90 °C for 36 h. The AC functionalized with oxygen moieties was thoroughly washed several times until the pH was neutral. Thus, the sample was dried overnight in an 80 °C oven to get BC.

To prepare f-CD, 8 g of thoroughly washed, dried and crushed PKS was mixed with 50 mL DI water. The mixture was transferred to a Teflon autoclave and set for hydrothermal treatment at 160 °C for 14 h. The supernatant solution was separated and centrifuged from the as-obtained sample at 9000 rpm. Lastly, the solution was once again filtered using 0.22 µm filter paper. This solution was then vacuum-dried to obtain f-CD.

2.2. Slurry Preparation

The slurry for the working electrodes was prepared in the ratio of 8:1:1, with active material, carbon black (~99%, Alfa Aesar, Haverhill, MA, USA) and a binder solution of 7 wt.% Polyvinylidene fluoride (PVDF, M_W ~530,000 pellets by GPC) dissolved in 1-methyl-2-pyrrolidinone (NMP-99%, Sigma-Aldrich, Hamburg, Germany). Initially, a dry mix of 0.4 g of active material with 0.05 g of carbon black was prepared by hand mixing in a mortar and drying in an oven at 120 °C for 1 h. Following, a wet mix of 0.714 g of PVDF was dissolved in NMP, and an additional NMP of 0.5 g was mixed thoroughly in a Thinky mixer (Thinky Corporation, ARE-310, Tokyo, Japan) for 30 min. The cooled dry mix was gradually added to the wet mix in four equal parts for 30 min. This protocol was followed for BC's slurry preparation. Various concentrations of f-CDs *viz.* 3, 5, 7 and 9 wt.% were tested by adding in BC, and the charge storage behaviour was studied using the galvanostatic charge-discharge (GCD) profile shown in Figure S1 in the Supporting Information to identify the optimum concentration of f-CDs. It was found that 7 wt.% f-CDs delivered the best performance. To prepare BC@f-CD, 7 wt.% of f-CD was added to the dry mix, reducing the corresponding amount of carbon black. To prepare BC@s-CNT, 0.4 wt.% of s-CNT (TUBALL™ BATT NMP 0.4% of SWCNT in 2% PVDF from OCSiAl Trading Shenzhen Co LTD., Shenzhen, China) was allowed to mix with 0.5 g of NMP before adding PVDF solution. The remaining procedure for slurry preparation is the same as stated before.

3. Results and Discussion

3.1. Physicochemical Properties of f-CD

The shape and size of f-CDs were primarily investigated using TEM images depicted in Figure 2a. The f-CDs show a quasi-spherical shape with 2–3 nm diameters. The higher resolution image of f-CDs in Figure 2b shows the lattice fringes with a spacing of 0.36 nm, revealing their partial graphitic nature. This feature is corroborated by the XRD pattern shown in Figure 2c, which shows a broad peak position around $2\theta = 24°$, corresponding to the (002) plane of graphitic carbon [29,30]. This peak substantiates the presence of turbostratic graphitic domains within the f-CDs. The Raman spectrum in Figure 2d presented additional insights into the structure. The spectrum shows two bands at 1352 and 1573 cm^{-1}, corresponding to the D-band and the G-band, respectively. The D-band arises from structural defects and disorder, while the G-band is associated with the sp^2-hybridized carbon domains [31,32]. The presence of the D-band suggests a higher density of active sites on the f-CDs, creating localized regions that can act as lithium adsorption sites, which could increase the reversible lithium storage capacity. The intensity ratio of the D-band to the G-band (I_D/I_G) is calculated to be 0.71, which aligns with the TEM and XRD analyses, further confirming the partial graphitic nature of the f-CDs.

The surface composition and chemical functionalities of the f-CDs were examined through XPS using the survey spectrum provided in Figure 2e. In addition to a prominent peak from carbon (C1s), the spectrum also indicates the presence of oxygen (O1s) and nitrogen (N1s) on the f-CD surface. The surface chemistry of f-CDs was further investigated using the high-resolution spectra of C1s, O1s, and N1s (included in the Supporting Information S1a–c). The deconvoluted C1s spectrum shown in Figure S2a reveals three distinct peaks at binding energies of 284.18 eV, 285.58 eV, and 287.69 eV, which are attributed to carbon species in -C-C/C=C, -C–O, and -C=O, respectively [33–35]. As seen in Figure S2b, the O1s spectrum demonstrates two significant peaks at 530.88 eV and 532.28 eV associated with -C=O (quinone) and C–OH (phenolic) groups, respectively [36–38]. These oxygen-containing functional groups enhance the surface polarity, enabling better lithium-ion adsorption and diffusion. The redox activity of -C=O groups contributes to faradaic reactions, thereby boosting the pseudocapacitance of the composite [39]. In contrast, the phenolic group can participate in hydrogen bonding and improve wettability, thus promoting better electrolyte penetration during battery operation. Similarly, the N1s spectrum, shown in Figure S2c, is resolved into two components, with peaks at 399.38 eV and 401.28 eV, attributed to pyrrolic nitrogen (N5) and quaternary nitrogen (N-Q) species, respectively [40]. The presence of pyrrolic nitrogen suggests the potential for modulating the charge carrier density, thereby enhancing interfacial capacitance. These surface functionalities play a crucial role in defining the electrochemical properties of the f-CDs.

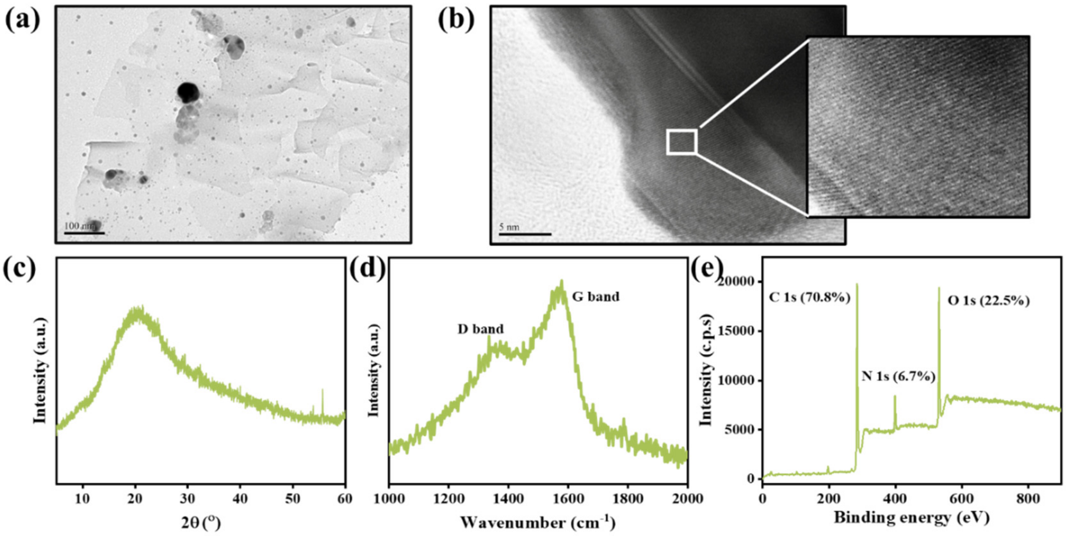

Figure 2. (**a**) The TEM image of f-CD, (**b**) The higher resolution TEM image with lattice fringes marked (**c**) XRD of f-CD, (**d**) Raman spectra of f-CD with two bands, (**e**) XPS survey scan of f-CD with peaks of carbon, nitrogen and oxygen.

3.2. Physicochemical Properties of BC, BC@s-CNT, and BC@f-CD

XRD analysis was carried out to evaluate the structure variation by adding s-CNT and f-CDs into BC, and the results are shown in Figure 3a. All samples exhibit two characteristic broad peaks centred at 2θ = ~24° and ~44°, corresponding to the (002) and (100) planes of amorphous carbon, respectively [41,42]. The similarity in the XRD patterns across all samples suggests that adding s-CNT or f-CDs does not significantly influence the crystal structure of BC. The consistent presence of the (002) and (100) planes for BC, BC@s-CNT, and BC@f-CD highlights that the core structural properties of the activated carbon remain intact despite the incorporation of s-CNT or f-CDs [43,44]. This indicates that the functionalization with f-CDs and the addition of s-CNT primarily enhance the surface characteristics of the composites without compromising the core structure of the BC.

Raman spectra were employed to analyze the structural and chemical changes of BC, BC@s-CNT and BC@f-CD, as provided in Figure 3b. For BC, the Raman spectrum exhibits the characteristic peaks of activated carbon appearing at ~1340 cm^{-1} (D-band) and ~1606 cm^{-1} (G-band) of disordered and graphitic carbon domains, respectively [45,46]. With the incorporation of f-CDs into BC, a minor shift of the D and G bands to lower wavenumbers, 1323 cm^{-1} and 1596 cm^{-1}, respectively, is observed. This shift suggests the presence of new interactions between the f-CDs and the BC matrix, potentially caused by charge transfer or interaction between the functional groups on the f-CDs and the carbon framework [47]. Such interactions may modify the electronic environment and lattice vibrations, influencing the Raman modes. Similarly, when s-CNT is added to the BC to form BC@s-CNT, the D and G bands are observed at ~1330 cm^{-1} and ~1595 cm^{-1}, respectively. The shift in these bands relative to pristine BC is attributed to localized strain and changes in the electronic structure introduced by the s-CNTs. The tubular structure of s-CNTs may exert mechanical strain on the BC matrix and promote enhanced π-π interactions, leading to slight alterations in the vibrational modes of the carbon lattice [48]. The degree of graphitization was determined by evaluating the ratio of the intensities of the D band to the G band, and the values are given in Figure 3b. The addition of f-CDs increases the degree of graphitization.

The variation in the surface area and pore distribution of BC, BC@s-CNT, and BC@f-CD was systematically analyzed using the gas adsorption-desorption technique and is shown in Figure 3c,d. The isotherms exhibit Type I and Type IV characteristics, with H4 hysteresis appearing in the relative pressure range of ~0.45–0.9 P/P_0. Such a profile indicates the presence of both micropores of diameter <2 nm and mesopores of diameter between 2–50 nm [49–51]. Typically, the hysteresis observed in Type IV isotherms is attributed to capillary condensation within mesopores, and the prominent increase in adsorption at low relative pressures indicates the significant contribution of micropores. A standard Type I isotherm has a broad pore size distribution comprised of substantial micropores and a narrow range of mesopores, as seen in the pore distribution curve in Figure 3d. As summarised in Table 1, the BET surface area and pore parameters reveal significant changes across the samples. The addition of f-CD increased the surface area of BC from 318 $m^2 \cdot g^{-1}$ to 624 $m^2 \cdot g^{-1}$ due to increased surface roughness and higher surface-volume-ratio of f-CDs. This improvement in surface area is aligned with prior literature on CDs enhancing the BET surface area of the host material, as provided in Table S1 in the Supporting Information. A minor increase in the micropore surface area from 0.58 $m^2 \cdot g^{-1}$ to 0.61 $m^2 \cdot g^{-1}$ indicates micropore utilization of f-CDs; however, a reduction in micropore volume from 0.77 $cm^3 \cdot g^{-1}$ to 0.53 $cm^3 \cdot g^{-1}$ is also observed. This suggests that although the total micropore volume decreases, the surface area of the remaining micropores becomes more efficient for ion interaction due to the nanostructured f-CDs. Moreover, the average pore diameter decreases slightly from 2.25 nm to 2.0 nm. The mesopores act as efficient channels for ion diffusion, providing accessible pathways for ions to move through the electrode [28,52,53].

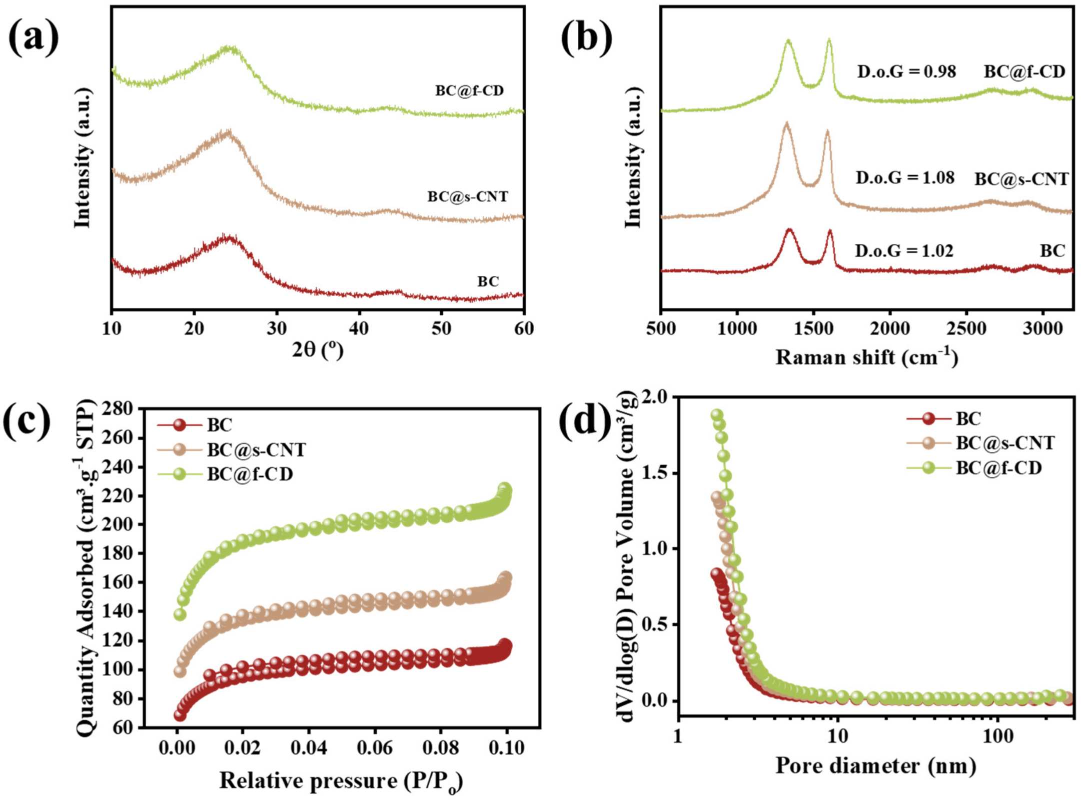

Figure 3. (**a**) Comparative XRD plot of BC, BC@s-CNT, and BC@f-CD (**b**) Comparative Raman spectra of BC, BC@s-CNT, and BC@f-CD (**c**) N_2 adsorption-desorption plot for BC, BC@s-CNT, and BC@f-CD (**d**) Pore distribution plot for BC, BC@s-CNT, and BC@f-CD.

Table 1. Consolidation of N_2 adsorption-desorption analysis.

Samples	**S_{BET} ($m^2 \cdot g^{-1}$)**	**S_{micro} ($m^2 \cdot g^{-1}$)**	**S_{micro}/S_{BET} ($m^2 \cdot g^{-1}$)**	**V_{total} ($cm^3 \cdot g^{-1}$)**	**V_{micro} ($cm^3 \cdot g^{-1}$)**	**$V_{micro/total}$ ($cm^3 \cdot g^{-1}$)**	**D (nm)**
BC	~318	~184	0.58	0.22	0.17	0.77	2.25
BC@s-CNT	~447	~272	0.61	0.25	0.13	0.52	2.24
BC@f-CD	~624	~386	0.62	0.34	0.18	0.53	2.20

S_{BET}—BET specific surface area; S_{micro}—micropore area; V_{total}—total pore volume; V_{micro}—micropore volume; D—average pore diameter.

The morphological and compositional features of the samples were systematically examined using FESEM and EDX, as depicted in Figure 4. Figure 4a highlights the porous architecture of BC with irregularly shaped and unevenly distributed pores. These pores form a disordered yet interconnected network, characteristic of BC, enabling ionic diffusion and storage [28]. The structure of BC@s-CNT is presented in Figures 4b and S3c, where s-CNTs are uniformly coated across the BC matrix and act as bridges connecting fragmented BC particles. At higher magnification (Figure 4c), the s-CNTs are seen to interweave between BC fragments, forming a well-integrated conductive framework. This conductive network is critical as it minimizes resistance and facilitates effective charge transport across the composite.

The compositional insights EDX provided are shown in Figure 4d,e. The BC sample primarily consists of carbon (71.92%) and oxygen (28.08%), with no nitrogen detected, consistent with the absence of nitrogen-based functionalities. Upon the incorporation of f-CDs, BC@f-CD exhibits a notable nitrogen content of 7.63%, in addition to carbon (67.24%) and oxygen (25.13%). The nitrogen is attributed to functional groups introduced by f-CDs, such as pyrrolic and quaternary nitrogen, which enhance surface reactivity, modulate charge density, and improve electrochemical performance. The uniform elemental distribution across BC (Figure S2) and BC@f-CD composite, as shown in the mapping images Figure 4f–h, shows the homogeneous integration of f-CDs into the BC structure. This uniformity ensures consistent electrochemical activity throughout the composite and indicates synergistic interactions between BC and f-CDs.

More conclusive information on the surface modification of BC with the conductive additives, the FTIR spectra of BC, BC@s-CNT, and BC@f-CD are presented in Figure S3e. BC is composed of three peaks: a broad peak at 3612 cm^{-1}, which corresponds to O–H stretching; a peak at 1727.9 cm^{-1}, which corresponds to C=O stretching; and a peak at 1565.6 cm^{-1}, which corresponds to C=C stretching. In addition to these peaks, BC@s-CNT presents a peak around 3222.4 cm^{-1}, attributed to C–H stretching. With the incorporation of f-CDs, peaks corresponding to nitrogen groups are observed in BC@f-CD. A distinct N–H stretching peak appears at 3421.1 cm^{-1}, along with a CN stretching band at 1216.8 cm^{-1}. The differences in peak intensities and shifts in BC@s-CNT and BC@f-CD compared to pristine BC suggest that the incorporation of s-CNTs and f-CDs introduces surface modifications.

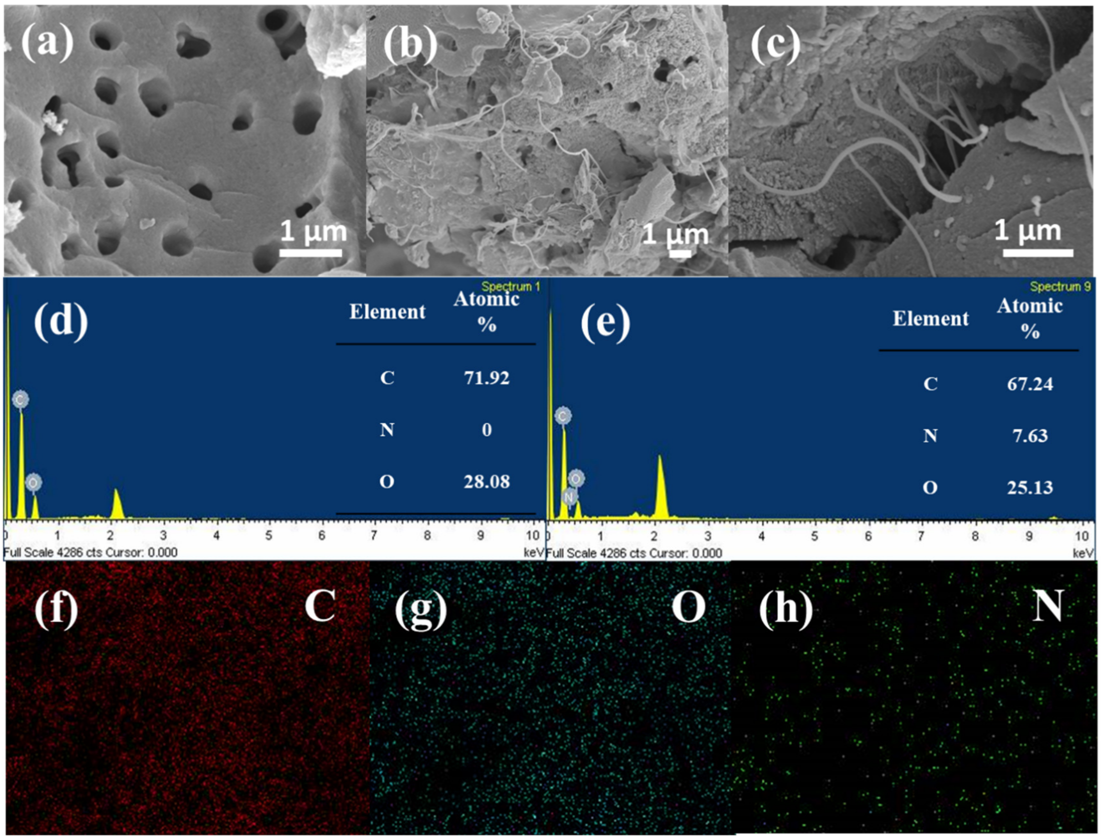

Figure 4. (**a**) The SEM image of BC (**b**,**c**) SEM image of BC@s-CNT showing s-CNT interconnecting fragmented BC particles (**d**,**e**) EDX spectra of BC and BC@f-CD (**f**–**h**) EDX mapping of BC@f-CD for carbon, oxygen and nitrogen.

3.3. Electrochemical Studies

Functional moieties in BC@f-CD significantly contribute to enhanced electrochemical performance by improving electrical conductivity and introducing active sites for redox reactions. To investigate this enhancement, DC polarisation measurements of all the samples were conducted to measure the conductivity (σ). The corresponding I-V curves, measured over a potential range of −2 to 2 V, are presented in Figure 5a. The results demonstrate a clear trend in conductivity, increasing progressively as BC < BC@s-CNT < BC@f-CD, with respective values of 5.3, 7.9, and 9.4 mS·cm^{-1}. The conductivity observed in BC@s-CNT can be attributed to the intrinsic conductivity of s-CNT. The delocalized π-electron system of s-CNTs facilitates efficient electron transport and effectively bridges fragmented carbon particles by establishing an interconnected conductive framework within the composite. In contrast, BC@f-CD exhibits the highest conductivity among the samples primarily due to the functional groups on the f-CDs. These groups introduce localized electron-rich sites, increasing the overall electron density and improving surface interactions. Additionally, the nanoscale dimensions of f-CDs allow them to effectively integrate within the carbon matrix, possibly passivating the defects in the carbon matrix, ensuring a more uniform and conductive network.

From the nitrogen adsorption-desorption studies, it was evident that BC@f-CD possesses a higher specific surface area compared to BC and BC@s-CNT. However, it is essential to note that not all the available surface area contributes directly to charge storage, as only the electrochemically active surface area (ECSA) participates in redox reactions and double-layer capacitance. The ECSA was estimated using the equation detailed in the Supporting Information (Supplementary Note S2) to assess this. The comparative results, shown in Figure 5b, reveal that incorporating s-CNT into BC increases the ECSA by ~17%, whereas adding f-CD enhances the ECSA significantly by ~47%. This pronounced improvement in the ECSA for BC@f-CD can be ascribed to the nano-dimensions of the f-CDs, which create additional active sites due to their high surface area-to-volume ratio. Furthermore, the functional groups present on the surface of the f-CDs, such as oxygen- and nitrogen-containing moieties, contribute to the enhancement of electrochemical activity by promoting faradaic reactions and improving the wettability of the electrode surface. These features collectively enable better utilization of the accessible surface area, facilitating efficient ion transport and charge storage. The increased ECSA directly translates into improved charge storability for BC@f-CD.

The cyclic voltammetric (CV) curves measured in the 2–4.3 V voltage range against a lithium anode revealed significant differences in charge storage behaviour among the cathodes, as shown in Figure 5c. The area enclosed by the CV profiles indicates that BC@f-CD exhibits the highest specific capacitance, suggesting its superior electrochemical performance. All samples show a redox peak between 3 and 3.4 V, consistent with previous reports where such peaks were attributed to oxygen functional groups present on the surface of BC [28]. In the case of BC@f-CD, the increased intensity of the redox peak suggests enhanced charge transfer, likely facilitated by additional oxygen and nitrogen functional groups introduced by the f-CDs. This enhancement indicates that the functionalized carbon dots contribute significantly to the redox activity, improving both the capacitive and faradaic charge storage mechanisms. CV plots at multiple scan rates, provided in Supporting Information Figure S4, reveal shifting redox peaks in all samples, indicative of diffusion-limited processes.

The GCD plots presented in Figure 5b were analyzed to evaluate the practical capacitance of the electrodes and showed a firm agreement with the CV results. The GCD curves, recorded at various current densities (provided in Supporting Information Figure S5), exhibit a quasi-triangular shape across all samples. This behaviour suggests a predominantly capacitive charge storage mechanism, with contributions from functional groups facilitating charge transfer. Specific capacitance values measured at 0.1 A·g^{-1} for BC, BC@s-CNT, and BC@f-CD were 90.4, 158.2, and 191.1 F·g^{-1}, respectively, indicating a significant improvement with the addition of s-CNT and f-CD. The enhanced capacitance of BC@s-CNT can be attributed to the conductive network formed by s-CNTs, which bridges fragmented BC particles and facilitates efficient charge transfer pathways. This resulted in a specific capacitance nearly 75% higher than that of pristine BC. In the case of BC@f-CD, introducing f-CDs increased the specific capacitance by ~97%, further improving charge storage performance. The improvement is primarily due to the additional surface functionalities and higher ECSA provided by f-CDs, which create more active sites for ion adsorption and enhance charge transfer kinetics. The specific capacitance at varying current densities, ranging from 0.2 A·g^{-1} to 5 A·g^{-1} and then back to 0.2 A·g^{-1}, is shown in Figure 5e. At the highest current density of 5 A·g^{-1}, BC retained only ~8% of its initial capacitance, indicating limited charge transfer and diffusion kinetics. In contrast, BC@s-CNT and BC@f-CD retained ~43% and ~54% of their capacitance, respectively. This higher retention at high current densities reflects the improved electronic conductivity of s-CNT and f-CD, facilitating faster ion and electron transport even under rapid charge/discharge conditions. Interestingly, upon returning to the lower current density of 0.2 A·g^{-1}, the capacitance retention was ~93%, ~99%, and ~97% for BC, BC@s-CNT, and BC@f-CD, respectively. The near-complete recovery demonstrates the structural stability of all electrodes.

The electrochemical impedance spectrum (EIS) of the cells after 24 h of incubation at room temperature after cell assembly, but prior to activation, is shown in Figure 5f. All the samples exhibit nearly similar impedance profiles, indicating comparable baseline behaviours across the systems. The experimental data were fitted using an equivalent circuit model to identify and analyze the various resistance components. Table 2 provides the fitting profiles and corresponding values; the fitted curves are provided in the Supporting Information in Figure S6.

The bulk resistance (R_b), which primarily arises from the ionic resistance of the electrolyte and the electronic resistance of the current collectors, was found to vary slightly among the samples. The R_b values for BC, BC@s-CNT, and BC@f-CD are 2.45 Ω, 2.79 Ω, and 2.40 Ω, respectively. The slightly higher R_b observed for BC@s-CNT may be due to the localized anisotropic diffusion pathways provided by s-CNT that hinder uniform ionic conduction through the electrolyte in the initial state. Conversely, the lowest R_b for BC@f-CD highlights the role of the f-CD in improving ionic conductivity by enhancing the interaction between the electrode and electrolyte [54]. The charge transfer resistance (R_{CT}), representing the resistance to electron transfer during redox reactions at the electrode/electrolyte interface, is lowest for BC@f-CD. This significant reduction in R_{CT} is attributed to the functional groups on f-CDs, which enhance the surface wettability of the electrode and facilitate better ionic interaction with the electrolyte [54]. Improved wettability leads to a more effective electrode/electrolyte interface, reducing the resistance to charge transfer. The higher R_{CT} values for BC and BC@s-CNT suggest less efficient interaction with the electrolyte in their pre-activated states.

The diffusional resistance (Z_{WR}) and diffusional time constant (Z_{WT}) are notably lower for BC@f-CD than the other samples. A lower diffusional time constant indicates faster ion transport within the electrode or electrolyte [50], highlighting the superior diffusion kinetics of BC@f-CD. This improvement can be attributed to the oxygen and nitrogen functional groups on the f-CDs, which enhance surface activity and create localized sites that reduce the energy barrier for ion diffusion. These functional groups also help maintain a well-connected pore network, facilitating smoother ion transport. In contrast, BC and BC@s-CNT exhibit higher Z_{WR} and longer Z_{WT}, suggesting less efficient ion transport pathways, likely due to their lower pore structures or fewer active sites in the initial state.

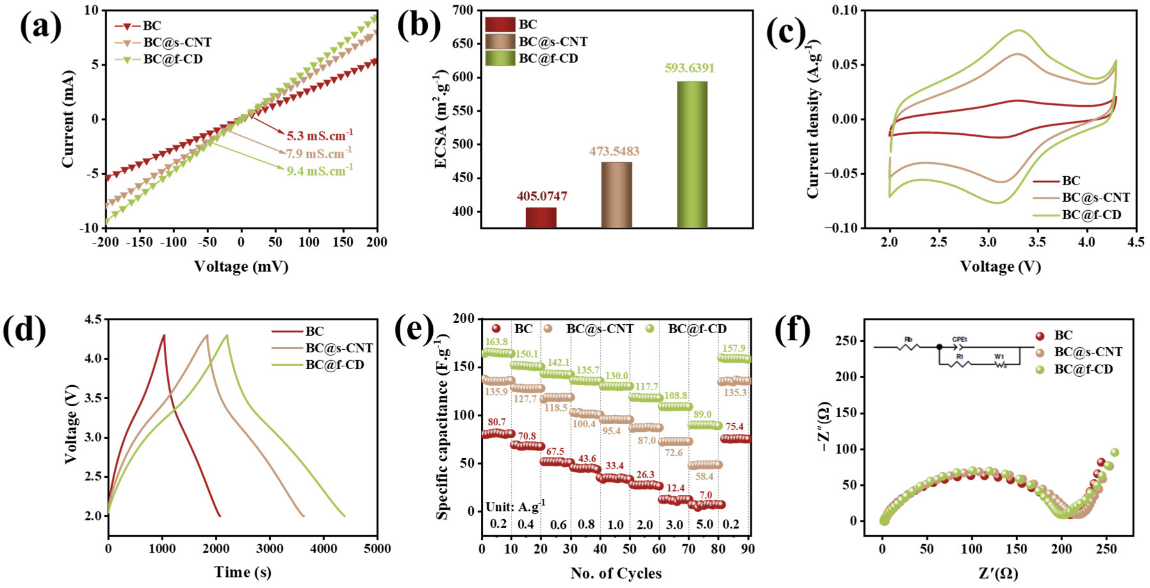

Figure 5. Comparative plots of BC, BC@s-CNT and BC@f-CD for (**a**) DC polarisation plot measured between −2 to 2 V, (**b**) Calculated ECSA, (**c**) CV plot measured at 0.05 $mV\cdot s^{-1}$, (**d**) GCD plots measured at 0.1 $A\cdot g^{-1}$ (**e**) Specific discharge capacitance of at current densities from 0.2 to 5 $A\cdot g^{-1}$ (**f**) EIS plots of fresh cells.

Table 2. Consolidation of EIS fitting parameters before activation.

Sample	R_b (Ω)	R_{CT} (Ω)	Z_W	
			R	T
BC	2.45	200	60.59	8.93
BC@s-CNT	2.79	204	52.29	9.68
BC@f-CD	2.40	190	29.32	4.93

3.3.1. Analysis of Charge Storable Behaviour

The charge storability mechanisms of the fabricated electrodes were initially examined using Lindström's power law equation, which differentiates between diffusion-dominated and adsorption-dominated processes [55,56]. As per the Lindström's equation at different scan rates (v):

$$i = av^b \quad (1)$$

$$\log i = \log a + b \log v \qquad (2)$$

where i represents the maximum current response at a particular v, a and b are variables determined from the plot between log$i$ and log$v$. The b value provides insight into the dominant mechanism, with a value near 0.5 indicating diffusion control and a value near 1 indicating surface control [57,58]. Figure 6a,d,g reveal b-values of 0.86, 0.84, and 0.79, respectively. The results suggest a progressive shift from adsorption-dominated behaviour in BC and BC@s-CNT to a more diffusion-dominated process in BC@f-CD. This trend indicates the influence of functional groups on f-CDs, which enhance electrolyte interactions, increase ion accessibility and improve diffusion dynamics within BC@f-CD.

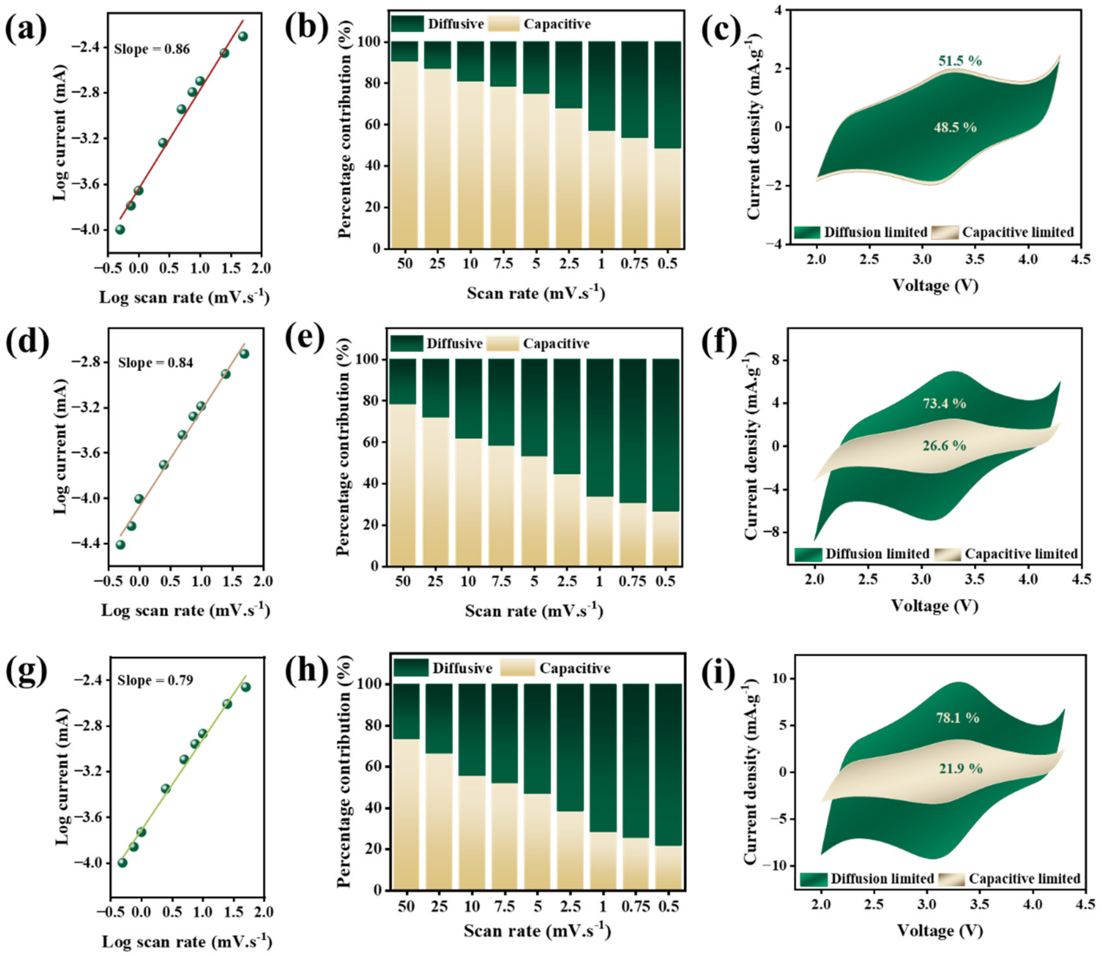

Figure 6. (**a**,**d**,**g**) shows the log v vs. log i, (**b**,**e**,**h**) percentage contribution of diffusion-limited and capacitive-limited charge storage at different scan rates (**c**,**f**, **i**) CV plots based on the percentage contributions for BC, BC@s-CNT and BC@f-CD.

To quantify the relative contributions of adsorption and diffusion, Dunn's method was applied using the equation:

$$i = k_1 v + k_2 \sqrt{v} \qquad (3)$$

The values obtained for k_1 and k_2 from the slope and intercept of the plot between $\frac{i}{\sqrt{v}}$ and $\sqrt{v}$ estimate the capacitive and diffusive behaviour, respectively [56]. Figure 6b,e,h revealed that diffusion dominates at lower scan rates due to improved ion interaction and bulk transport facilitated by the hierarchical structure and functional moieties. At the lowest scan rate of 0.5 mV·s^{-1}, the diffusion contribution increased from ~49% in BC to ~73% with s-CNT addition (Figure 6c,f). However, the anisotropic diffusion behaviour and the tendency of s-CNT to aggregate into dense bundles slightly limited ion accessibility [19]. In contrast, BC@f-CD achieved the highest diffusion contribution both at low and high scan rates (~78%), as shown in Figure 6i, due to the combined effects of surface functionalities and the partially graphitic nature of f-CDs, which provided localized lattice sites for ion transport. This higher capacitive limited performance of BC@s-CNT could be the reason for the higher capacitance retention at 0.2 A·g^{-1}.

In fact, the observed increase in the diffusion contribution in BC@f-CD can be attributed to many factors. The oxygen- and nitrogen-based functional groups on f-CDs introduce numerous polar sites that interact strongly with electrolyte ions, facilitating adsorption at the electrode surface and diffusion into the bulk material. Additionally, the nano-dimensionality of f-CDs ensures a high surface-to-volume ratio, exposing more active sites for redox reactions and reducing ion diffusion distances. The graphitic domains in f-CDs contribute to enhanced ionic transport kinetics by providing low-energy pathways for ion diffusion. In contrast, the porous structure formed by integrating f-CDs into the BC matrix facilitates interconnected channels that improve ion mobility. These structural and functional features work synergistically to optimize electronic and ionic conductivity, boosting the diffusion-dominated charge storage observed in BC@f-CD.

3.3.2. Cyclic Stability Studies

Long-term cycling stability was evaluated for the fabricated devices over 5000 charge-discharge cycles at a fixed current density of 0.6 A·g^{-1}, summarising the results in Figure 7. The performance of each sample demonstrated significant differences in capacitance retention and Coulombic efficiency. For BC, shown in Figure 7a, severe capacitance fading was observed after 5000 cycles, retaining only ~50% of the initial value. A similar observation has been observed in systems with activated carbon electrodes tested in organic electrolytes [59–61]. Additionally, the Coulombic efficiency fluctuated significantly throughout the cycling, suggesting instability in the electrochemical processes and possible material degradation. In contrast, BC@s-CNT, presented in Figure 7b, exhibited improved cycling stability, retaining ~83% of its initial capacitance after 5000 cycles. The Coulombic efficiency remained much more stable, attributed to the improved electronic conductivity and conductive pathways provided by s-CNTs, which mitigate electrode degradation and enhance charge transfer kinetics. Slightly better performance was observed for BC@f-CD, shown in Figure 7c, with a capacitance retention of ~86%. The enhanced performance of BC@f-CD is attributed to the functional groups of f-CDs, which improve electrode wettability, promote better ion interaction, and stabilize the electrode-electrolyte interface.

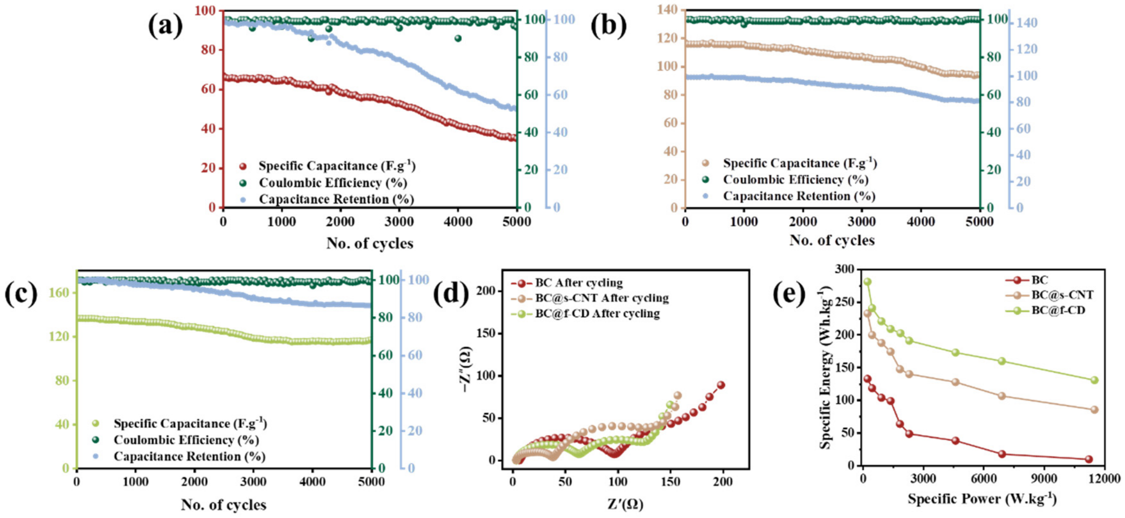

Figure 7. (**a**–**c**) Plots showcasing capacitance fading, capacitance retention and coulombic efficiency of BC, BC@s-CNT and BC@f-CD (**d**) Post cycling EIS of all the samples (**e**) Ragone plot drawn for different current densities of each sample.

Post-cycling EIS analysis, shown in Figure 7d, and the corresponding parameters from circuit fitting in Table 3 provide insights into the resistance changes after cycling. A new semicircle appeared in the mid-frequency range of the Nyquist plot, representing the formation of a solid electrolyte interface (SEI) [62]. The SEI resistance (R_{SEI}) was highest for BC, reflecting significant electrolyte decomposition and instability at the electrode-electrolyte interface, adversely impacting device durability. In contrast, BC@s-CNT exhibited the lowest R_{SEI}, owing to the robust structural network formed by s-CNTs, which reduces SEI formation by limiting direct contact between the electrolyte and the active material. Meanwhile, BC@f-CD showed a moderate R_{SEI} of 62 Ω. Additional resistive components such as R_{CT}, Z_{WR} and Z_{WT} were found to be lowest for BC@f-CD. This suggests that incorporating f-

CDs enhances ion transport and charge transfer processes due to their high surface area, functional groups, and partial graphitic nature, optimizing electron pathways and ionic interactions.

Table 3. Consolidation of EIS fitting parameters after 5000 cycles.

Sample	R_b (Ω)	R_{SEI} (Ω)	R_{CT} (Ω)	Z_W	
				R	T
BC	2.45	91.93	61.62	122.2	23.17
BC@s-CNT	2.79	34.52	86.57	94.41	22.17
BC@f-CD	2.40	62.00	52.74	37.03	7.45

The specific energy and specific power of the fabricated devices were evaluated and compared using a Ragone plot, as shown in Figure 7e. The BC@f-CD device demonstrated a maximum specific energy of ~281 Wh·kg^{-1} and a maximum specific power of 11.5 kW·kg^{-1}, showcasing its significantly superior performance. Compared to BC, this represents a 111% increase in specific energy and a slight increment of 2.49% increase in specific power, emphasizing the transformative role of f-CDs in enhancing device performance. Similarly, BC@s-CNT showed an improvement of 75% in specific energy. However, BC@s-CNT demonstrated the same specific power as that of BC@f-CD. These improvements establish BC@f-CD as a promising and cost-effective additive that can replace s-CNTs and deliver high specific power without compromising specific power. Table 4 compares the previous literature with the electrochemical performance of BC@f-CD.

Table 4. Table comparing previous literature with the current work.

Device	Voltage Window (V)	Specific Capacitance (F·g^{-1})	Specific Energy (Wh·kg^{-1})	Specific Power (W·kg^{-1})	Capacitance Retention	Reference
Functionalized AC	2.0–4.5	165	-	-	70% over 500 cycles @0.1 A·g^{-1}	[14]
AC coated with cobalt film	2.0–4.5	145	125	3200	100% over 500 cycles @0.1 A·g^{-1}	[16]
AC from rice husk	2.8–4.2	140	35		75% over 10000 cycles	[7]
AC from PKS	2.0–4.0	120	66.7	3450	95% over 500 cycles @0.1 A·g^{-1}	[15]
AC from coconut rachis	2.0–4.0	104	76	7600	84% over 5000 cycles @1 A·g^{-1}	[13]
AC	2.2–3.8	191	8.2	-	95% over 8000 cycles @30C	[8]
BC@f-CD	2.0–4.0	191	280	11,500	86% over 5000 cycles @0.6 A·g^{-1}	This work

To summarise, the charge storage mechanism in BC, BC@s-CNT, and BC@f-CD cathodes involves the coordinated movement and interaction of Li^+ and PF_6^- ions within the 1 M $LiPF_6$ EC: DEC electrolyte. During charging, PF_6^- ions are adsorbed onto the cathode, forming an electrical double layer (EDL). In BC, the charge storage primarily relies on the physical adsorption of PF_6^- ions within the micropores and mesopores, limited by the lack of functional groups and a relatively low surface area, resulting in moderate specific energy and power. In BC@s-CNT, the conductive network formed by s-CNTs enhances electron transport. It facilitates faster adsorption of PF_6^- ions, improving specific power but still lacking the chemical enhancement necessary for significant faradaic contributions. In contrast, BC@f-CD benefits from the presence of oxygen and nitrogen functional groups introduced by the f-CDs. These promote strong electrostatic and chemical interactions with PF_6^- ions, enabling partial faradaic reactions in addition to EDL formation. The optimized pore structure and increased surface area of BC@f-CD further enhance ion storage and diffusion efficiency. Li^+ ions are stripped from the anode during discharging, while PF_6^- ions desorb from the cathode. In BC, the desorption is governed by weak physical interactions, leading to slower ion release and limited power density. In BC@s-CNT, the conductive pathways provided by s-CNTs reduce ion diffusion resistance, enabling faster ion release. However, in BC@f-CD, the desorption is facilitated by the functional groups, ensuring uniform and efficient ion release while maintaining strong ion interactions, leading to superior charge storage, higher energy density, and stable cycling performance. Thus, the synergy between capacitive and faradaic mechanisms in BC@f-CD, combined with its optimized ion transport pathways, distinguishes it as this system's most efficient cathode material. The charge storage mechanism in each of the cathode materials is depicted in Figure 8a–c.

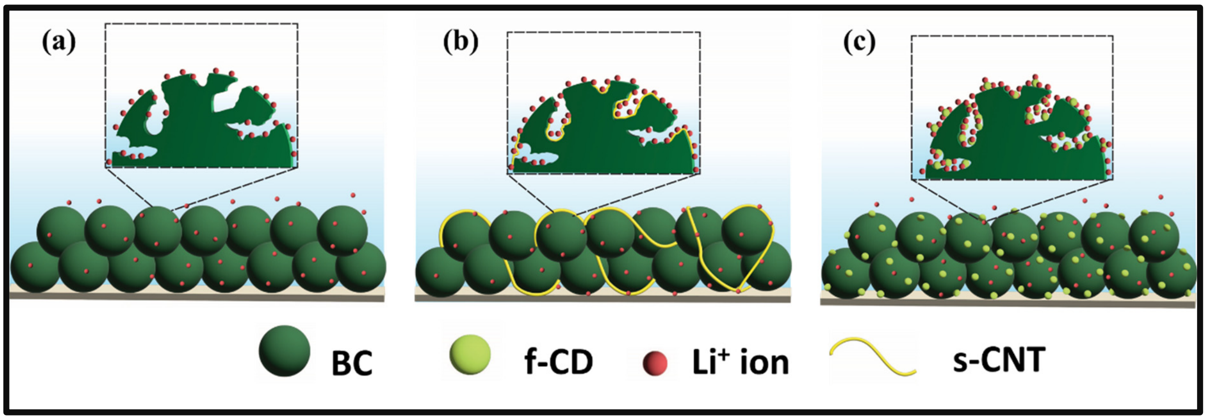

Figure 8. Schematic representation of charge storage mechanism in (**a**) BC, (**b**) BC@s-CNT and (**c**) BC@f-CD. Compared to BC and BC@s-CNT, BC@f-CD shows improved diffusion and enhanced charge storability.

5. Conclusions

In conclusion, this study analyses the effectiveness of f-CDs as a cheap alternative for s-CNTs to enhance the performance of BC in LMCs. The f-CDs, synthesized from palm kernel shells, introduce oxygen and nitrogen functional groups, optimize pore structure, and increase surface area, significantly improving ion adsorption and charge storage. Gas adsorption-desorption studies reveal a refined microporous and mesoporous structure with a surface area increase from 318 $m^2 \cdot g^{-1}$ for BC to 624 $m^2 \cdot g^{-1}$ for BC@f-CD, facilitating efficient ion diffusion and adsorption. Long-term cycling tests show retention of ~86% after 5000 cycles for BC@f-CD, with reduced resistance (R_{CT}, R_{SEI}) and enhanced ionic transport compared to BC and BC@s-CNT. Electrochemical studies demonstrate that BC@f-CD exhibits a specific energy of 280.8 $Wh \cdot kg_{cathode}^{-1}$ and a specific power of 11.5 $W \cdot kg_{cathode}^{-1}$, reflecting improvements of 111% and 2.5%, respectively, compared to BC. Thus, these results show that f-CDs are an alternative for s-CNTs with higher electrochemical figures of merit economically and sustainably.

Supplementary Materials

The following supporting information can be downloaded at: https://www.sciltp.com/journals/matsus/2025/1/646/s1, Supplementary Note S1: Material characterizations, electrochemical characterizations; Supplementary Note S2: Equations used for calculating an electrochemical figure of merits; Figure S1: GCD plot comparing the various concentrations of f-CD addition in BC; Figure S2: Deconvoluted XPS spectra of (a) C1s (b) N1s and (c) O1s.; Figure S3: SEM images of (a) BC@s-CNT and (b) BC@f-CD. The f-CD particles appear to be aggregated due to the SEM resolution limitation. EDX mapping of BC for (c) carbon and (d) oxygen, (e) comparative FTIR of BC, BC@s-CNT and BC@f-CD; Figure S4: CV plots at different scan rates for (a) BC, (b) BC@s-CNT, and (c) BC@f-CD; Figure S5: GCD plots at different current densities for (a) BC, (b) BC@s-CNT, and (c) BC@f-CD; Figure S6: EIS fitted data for (a) BC, (b) BC@s-CNT, and (c) BC@f-CD, before cycling. EIS fitted data for (d) BC, (e) BC@s-CNT, and (f) BC@f-CD after cycling. Table S1: Literature comparing the BET surface area of materials before and after the addition of CDs. References [63–68] are cited in the supplementary materials.

Author Contributions

G.G.: Investigation, Data curation, Methodology, Validation, Visualization, Formal analysis, Writing—original draft, Writing—review & editing. G.R.D.: Data curation, Investigation, Formal analysis; V.S.: Data curation, Formal analysis, Validation, Writing—review & editing; I.I.M.: Funding acquisition, Supervision; C.-C.Y.: Methodology, Funding acquisition, Validation, Supervision, Resources, Project administration; R.J.: Conceptualization, Validation, Funding acquisition, Supervision, Resources, Project administration, Writing—review & editing. All authors have read and agreed to the published version of the manuscript.

Funding

This research was funded by the Post-graduate Research Scheme (PGRS, UMP.05.02/26.10/03/03/PGRS2003124. G.G.) and the Taiwan Ministry of Education for the funding through the Taiwan Experience Education Program (TEEP@AsiaPlus) and Battery Research Centre for Green Energy (BRCGE) of the Ming Chi University of Technology.

Data Availability Statement

The datasets generated during and/or analyzed during the current study are available from the corresponding author upon reasonable request.

Conflicts of Interest

The authors declare no conflict of interest.

References

1. Khan, M.I.; Gilani, R.; Hafeez, J.; et al. Advantages and disadvantages of lithium-ion batteries. In *Nanostructured Lithium-ion Battery Materials*; Elsevier: Amsterdam, The Netherlands, 2025; pp. 47–64.
2. Kim, T.; Song, W.; Son, D.-Y.; et al. Lithium-ion batteries: Outlook on present, future, and hybridized technologies. *J. Mater. Chem. A* **2019**, *7*, 2942–2964.
3. Wu, J.; Cao, Y.; Zhao, H.; et al. The critical role of carbon in marrying silicon and graphite anodes for high-energy lithium-ion batteries. *Carbon Energy* **2019**, *1*, 57–76.
4. Acebedo, B.; Morant-Miñana, M.C.; Gonzalo, E.; et al. Current Status and Future Perspective on Lithium Metal Anode Production Methods. *Adv. Energy Mater.* **2023**, *13*, 2203744, https://doi.org/10.1002/aenm.202203744.
5. Yang, L.; Hagh, N.M.; Macciomei, E.; et al. Challenges and Opportunities in Lithium Metal Battery Technology. *J. Electrochem. Soc.* **2024**, *171*, 060504.
6. Cheng, X.-B.; Zhang, R.; Zhao, C.-Z.; et al. Toward safe lithium metal anode in rechargeable batteries: A review. *Chem. Rev.* **2017**, *117*, 10403–10473.
7. Yerdauletov, M.S.; Nazarov, K.; Mukhametuly, B.; et al. Characterization of activated carbon from rice husk for enhanced energy storage devices. *Molecules* **2023**, *28*, 5818.
8. Shaibani, M.; Abedin, M.J.; Sharifzadeh Mirshekarloo, M.; et al. New Class of High-Energy, High-Power Capacitive Devices Enabled by Stabilized Lithium Metal Anodes. *ACS Appl. Mater. Interfaces* **2023**, *15*, 37454–37466.
9. Tan, L.; Huang, X.; Yin, T.; et al. A 5 V ultrahigh energy density lithium metal capacitor enabled by the fluorinated electrolyte. *Energy Storage Mater.* **2024**, *71*, 103692, https://doi.org/10.1016/j.ensm.2024.103692.
10. Liu, B.; Chen, J.; Yang, B.; et al. Boosting the performance of lithium metal capacitors with a Li composite anode. *J. Mater. Chem. A* **2021**, *9*, 10722–10730.
11. Liu, B.; Chen, J.; Yang, B.; et al. An ultrahigh-energy-density lithium metal capacitor. *Energy Storage Mater.* **2021**, *42*, 154–163.
12. Zhong, Q.; Liu, B.; Yang, B.; et al. Flexible lithium metal capacitors enabled by an in situ prepared gel polymer electrolyte. *Chin. Chem. Lett.* **2021**, *32*, 3496–3500.
13. Shah, N.; Ling, J.; Misnon, I.I.; et al. A simple formula to fabricate high performance lithium metal capacitors. *J. Energy Storage* **2025**, *105*, 114682.
14. Vijayan, B.L.; Yasin, A.; Misnon, I.I.; et al. Lithium-ion adsorption on surface modified porous carbon. *J. Energy Storage* **2023**, *71*, 108221, https://doi.org/10.1016/j.est.2023.108221.
15. Vijayan, B.L.; Misnon, I.I.; Anilkumar, G.M.; et al. Void-size-matched hierarchical 3D titania flowers in porous carbon as an electrode for high-density supercapacitive charge storage. *J. Alloys Compd.* **2021**, *858*, 157649, https://doi.org/10.1016/j.jallcom.2020.157649.
16. Vijayan, B.L.; Misnon, I.I.; Karuppaiah, C.; et al. Thin metal film on porous carbon as a medium for electrochemical energy storage. *J. Power Sources* **2021**, *489*, 229522, https://doi.org/10.1016/j.jpowsour.2021.229522.
17. Jiang, T.; Amadei, C.A.; Gou, N.; et al. Toxicity of single-walled carbon nanotubes (SWCNTs): Effect of lengths, functional groups and electronic structures revealed by a quantitative toxicogenomics assay. *Environ. Sci. Nano* **2020**, *7*, 1348–1364.
18. Raphey, V.; Henna, T.; Nivitha, K.; et al. Advanced biomedical applications of carbon nanotube. *Mater. Sci. Eng. C* **2019**, *100*, 616–630.
19. Izadi-Najafabadi, A.; Futaba, D.N.; Iijima, S.; et al. Ion diffusion and electrochemical capacitance in aligned and packed single-walled carbon nanotubes. *J. Am. Chem. Soc.* **2010**, *132*, 18017–18019.
20. Dong, Q.; Nasir, M.Z.M.; Pumera, M. Semi-conducting single-walled carbon nanotubes are detrimental when compared to metallic single-walled carbon nanotubes for electrochemical applications. *Phys. Chem. Chem. Phys.* **2017**, *19*, 27320–27325.
21. Ganesh, G.; Misnon, I.I.; Jose, R. Solvothermal synthesis of green fluorescent carbon dots from palm kernel shells. *Mater. Today Proc.* **2023**, https://doi.org/10.1016/j.matpr.2023.02.332.
22. Shaker, M.; Ng, S.; Ghazvini, A.A.S.; et al. Carbon/graphene quantum dots as electrolyte additives for batteries and supercapacitors: A review. *J. Energy Storage* **2024**, *85*, 111040.

23. Jiang, Z.; Guan, L.; Xu, X.; et al. Applications of carbon dots in electrochemical energy storage. *ACS Appl. Electron. Mater.* **2022**, *4*, 5144–5164.
24. Li, S.; Luo, Z.; Tu, H.; et al. N,S-codoped carbon dots as deposition regulating electrolyte additive for stable lithium metal anode. *Energy Storage Mater.* **2021**, *42*, 679–686.
25. Arumugam, P.; Elumali, S.R.; Raman, K.; et al. Green Synthesis of Corn Cob Derived Carbon Quantum Dots and Its Applications as Electrolyte Additive for Lithium-Metal Batteries. *ECS Trans.* **2022**, *107*, 16547.
26. Yang, S.; Xu, Z.; Wang, S.; et al. Hydrophilic and nanocrystalline carbon quantum dots enable highly reversible zinc-ion batteries. *Green Chem.* **2024**, *26*, 7293–7301.
27. Ganesh, G.; Sunil, V.; Ling, J.; et al. Carbon dots as a sustainable electrolyte enhancer in aqueous alkaline electrochemical capacitors. *J. Energy Storage* **2024**, *94*, 112465.
28. Sunil, V.; Yasin, A.; Pal, B.; et al. Tailoring the charge storability of commercial activated carbon through surface treatment. *J. Energy Storage* **2022**, *55*, 105809.
29. Liu, C.; Wen, M.; Zhou, X.; et al. Starch-Derived Carbon Dots with Enhanced Photoluminescence and Tunable Emission for Multilevel Anticounterfeiting. *ACS Sustain. Chem. Eng.* **2024**, *12*, 12354–12364.
30. Luo, H.; Lari, L.; Kim, H.; et al. Structural evolution of carbon dots during low temperature pyrolysis. *Nanoscale* **2022**, *14*, 910–918.
31. Kim, K.; Chokradjaroen, C.; Saito, N. Solution plasma: New synthesis method of N-doped carbon dots as ultra-sensitive fluorescence detector for 2, 4, 6-trinitrophenol. *Nano Express* **2020**, *1*, 020043.
32. Yu, R.; Liang, S.; Ru, Y.; et al. A facile preparation of multicolor carbon dots. *Nanoscale Res. Lett.* **2022**, *17*, 32.
33. Wang, S.; Liu, S.; Zhang, J.; et al. Highly fluorescent nitrogen-doped carbon dots for the determination and the differentiation of the rare earth element ions. *Talanta* **2019**, *198*, 501–509.
34. Zulfajri, M.; Gedda, G.; Chang, C.-J.; et al. Cranberry beans derived carbon dots as a potential fluorescence sensor for selective detection of Fe3+ ions in aqueous solution. *ACS Omega* **2019**, *4*, 15382–15392.
35. Wang, J.; Xiao, L.; Wen, S.; et al. Hierarchically porous SiO 2/C hollow microspheres: A highly efficient adsorbent for Congo Red removal. *RSC Adv.* **2018**, *8*, 19852–19860.
36. Zhang, M.; Wang, W.; Liang, X.; et al. Promoting operating voltage to 2.3 V by a superconcentrated aqueous electrolyte in carbon-based supercapacitor. *Chin. Chem. Lett.* **2021**, *32*, 2217–2221.
37. Meng, F.; Song, M.; Wei, Y.; et al. The contribution of oxygen-containing functional groups to the gas-phase adsorption of volatile organic compounds with different polarities onto lignin-derived activated carbon fibers. *Environ. Sci. Pollut. Res.* **2019**, *26*, 7195–7204.
38. Rezaei, A.; Hadian-Dehkordi, L.; Samadian, H.; et al. Pseudohomogeneous metallic catalyst based on tungstate-decorated amphiphilic carbon quantum dots for selective oxidative scission of alkenes to aldehyde. *Sci. Rep.* **2021**, *11*, 4411.
39. Yu, M.; Zhang, S.; Chen, Y.; et al. A green method to reduce graphene oxide with carbonyl groups residual for enhanced electrochemical performance. *Carbon* **2018**, *133*, 101–108.
40. Liu, Y.; Zhu, C.; Gao, Y.; et al. Biomass-derived nitrogen self-doped carbon dots via a simple one-pot method: Physicochemical, structural, and luminescence properties. *Appl. Surf. Sci.* **2020**, *510*, 145437.
41. Sunil, V.; Salehan, S.S.; Ganesh, G.; et al. Nanoarchitectonics with improved supercapacitive performance of jering-derived porous activated carbon electrodes in aqueous electrolyte. *Ionics* **2024**, *30*, 5767–5776.
42. Misnon, I.I.; Zain, N.K.M.; Jose, R. Conversion of oil palm kernel shell biomass to activated carbon for supercapacitor electrode application. *Waste Biomass Valorization* **2019**, *10*, 1731–1740.
43. Sahoo, S.; Satpati, A.K.; Sahoo, P.K.; et al. Incorporation of Carbon Quantum Dots for Improvement of Supercapacitor Performance of Nickel Sulfide. *ACS Omega* **2018**, *3*, 17936–17946. https://doi.org/10.1021/acsomega.8b01238.
44. Li, Q.; Chen, J.; Zhang, L. Nickel-cobalt oxide coated CNTs as additives of activated carbon electrode for high-performance supercapacitors. In Proceedings of the 2013 13th IEEE International Conference on Nanotechnology (IEEE-NANO 2013), Beijing, China, 5–8 August 2013; pp. 348–351.
45. Schopf, D.; Es-Souni, M. Supported porous carbon and carbon–CNT nanocomposites for supercapacitor applications. *Appl. Phys. A* **2016**, *122*, 203.
46. Tang, J.; Chen, S.; Jia, Y.; et al. Carbon dots as an additive for improving performance in water-based lubricants for amorphous carbon (aC) coatings. *Carbon* **2020**, *156*, 272–281.
47. Kumar, V.B.; Borenstein, A.; Markovsky, B.; et al. Activated carbon modified with carbon nanodots as novel electrode material for supercapacitors. *J. Phys. Chem. C* **2016**, *120*, 13406–13413.
48. Zhang, P.; Fan, J.; Wang, Y.; et al. Insights into the role of defects on the Raman spectroscopy of carbon nanotube and biomass-derived carbon. *Carbon* **2024**, *222*, 118998.
49. Bläker, C.; Muthmann, J.; Pasel, C.; et al. Characterization of activated carbon adsorbents–state of the art and novel approaches. *ChemBioEng Rev.* **2019**, *6*, 119–138.

50. Sunil, V.; Pal, B.; Misnon, I.I.; et al. Characterization of supercapacitive charge storage device using electrochemical impedance spectroscopy. *Mater. Today Proc.* **2021**, *46*, 1588–1594.
51. Pal, B.; Yasin, A.; Sunil, V.; et al. Enhancing the materials circularity: From laboratory waste to electrochemical capacitors. *Mater. Today Sustain.* **2022**, *20*, 100221.
52. Wang, D.; Qiu, J.; Inui, N.; et al. Between Promise and Practice: A Comparative Look at the Energy Density of Li Metal-Free Batteries and Li Metal Batteries. *ACS Energy Lett.* **2023**, *8*, 5248–5252. https://doi.org/10.1021/acsenergylett.3c02105.
53. An, G.-H.; Kim, H.; Ahn, H.-J. Improved Ionic Diffusion through the Mesoporous Carbon Skin on Silicon Nanoparticles Embedded in Carbon for Ultrafast Lithium Storage. *ACS Appl. Mater. Interfaces* **2018**, *10*, 6235–6244, https://doi.org/10.1021/acsami.7b15950.
54. Kumar, S.; Goswami, M.; Singh, N.; et al. Exploring carbon quantum dots as an aqueous electrolyte for energy storage devices. *J. Energy Storage* **2022**, *55*, 105522.
55. Lindström, H.; Södergren, S.; Solbrand, A.; et al. Li^+ ion insertion in TiO_2 (anatase). 2. Voltammetry on nanoporous films. *J. Phys. Chem. B* **1997**, *101*, 7717–7722.
56. Jorn-am, T.; Supchocksoonthorn, P.; Pholauyphon, W.; et al. Quasi-solid, bio-renewable supercapacitors based on cassava peel and cassava starch and the use of carbon dots as performance enhancers. *Energy Fuels* **2022**, *36*, 7865–7877.
57. Raavi, R.; Archana, S.; Reddy, P.A.; et al. Performances of dual carbon multi-ion supercapacitors in aqueous and non-aqueous electrolytes. *Energy Adv.* **2023**, *2*, 385–397.
58. Schoetz, T.; Gordon, L.; Ivanov, S.; et al. Disentangling faradaic, pseudocapacitive, and capacitive charge storage: A tutorial for the characterization of batteries, supercapacitors, and hybrid systems. *Electrochim. Acta* **2022**, *412*, 140072.
59. Eleri, O.E.; Huld, F.; Pires, J.; et al. Revealing mechanisms of activated carbon capacity fade in lithium-ion capacitors. *Electrochim. Acta* **2023**, *453*, 142359, https://doi.org/10.1016/j.electacta.2023.142359.
60. Zhang, T.; Fuchs, B.; Secchiaroli, M.; et al. Electrochemical behavior and stability of a commercial activated carbon in various organic electrolyte combinations containing Li-salts. *Electrochim. Acta* **2016**, *218*, 163–173, https://doi.org/10.1016/j.electacta.2016.09.126.
61. Eleri, O.E.; Lou, F.; Yu, Z. Lithium-Ion Capacitors: A Review of Strategies toward Enhancing the Performance of the Activated Carbon Cathode. *Batteries* **2023**, *9*, 533.
62. Choi, W.; Shin, H.-C.; Kim, J.M.; et al. Modeling and applications of electrochemical impedance spectroscopy (EIS) for lithium-ion batteries. *J. Electrochem. Sci. Technol.* **2020**, *11*, 1–13